**"8th Workshop on Three-Dimensional Modelling of
Seismic Waves Generation, Propagation and their Inversion"**

25 September - 7 October 2006

Crust and Mantle of the Tien Shan from Data of the Receiver Function Tomography

Lev Vinnik

**Institute of Physics of the Earth
Moscow, Russia**

Crust and Mantle of the Tien Shan from Data of the Receiver Function Tomography

L. P. Vinnik[a], **I. M. Aleshin**[a], **M. K. Kaban**[a], **S. G. Kiselev**[a],
G. L. Kosarev[a], **S. I. Oreshin**[a], **and Ch. Reigber**[b]

[a] *Schmidt Institute of Physics of the Earth, Russian Academy of Sciences,*
Bol'shaya Gruzinskaya ul. 10, Moscow, 123995 Russia
[b] *GeoForchungsZentrum Potsdam, Potsdam, Germany*
Received February 13, 2006

Abstract—A 3-D velocity model of the Tien Shan crust and upper mantle is constructed through the inversion of the receiver functions of *P* and *S* waves together with teleseismic traveltime anomalies at nearly 40 local seismic stations. It is found that in the vast central region, where no strong earthquakes have been known over the past century, the *S* wave velocity at depths of 10–35 km is lower than in adjacent regions by up to 10%. These data are evidence for mechanical weakness of the crust preventing the accumulation of elastic energy. Apparently, the lower velocity and the weakness of the crust are due to the presence of water. The weakness of the crust is one of the possible reasons for the strain localization responsible for the formation of the present Tien Shan but can also be due in part to the young orogenesis. The crustal thickness is largest (about 60 km) in the Tarim–Tien Shan junction zone. The crust–mantle boundary in this region descends by a jump as a result of an increase in the lower crust thickness. This is probably due to the underthrusting of the Tien Shan by the Tarim lithosphere. This causes the mechanically weak lower crust of the Tarim to delaminate and accumulate in nearly the same way as an accretionary prism during the subduction of oceanic lithosphere. In the upper mantle, the analysis has revealed a low velocity anomaly, apparently related to basaltic outflows of the Upper Cretaceous–Early Paleogene. The Cenozoic Bachu uplift in the northern Tarim depression is also associated with the low velocity anomaly. The Naryn depression is characterized by a high velocity in the upper mantle and can be interpreted as a fragment of an ancient platform.

PACS numbers: 91.30.Ab

DOI: 10.1134/S1069351306080027

1. INTRODUCTION

The Tien Shan is an intracontinental mountainous structure that is the largest in the world and the most active. The ancient Tien Shan formed as a result of the collision of a few continental fragments in the Paleozoic [Burtman, 1975]; however, the resulting topography was destroyed in the Mesozoic. Tectonic activity in the Southern Tien Shan resumed at about 20 Ma [Sobel and Dumitru, 1997], apparently, due to the collision of India with Eurasia [Molnar and Tapponnier, 1975]. At present, the Tien Shan is shortening in the N–S direction at a rate of about 20 mm/yr [Abdrakhmatov et al., 1996; Reigber et al., 2001], and this shortening is accommodated by several large faults separated by rigid blocks [Thompson et al., 2002]. Its total shortening amounts to a few tens of kilometers [Makarov, 1977; Abdrakhmatov et al., 2001]; with the present shortening rate, this value can be attained over approximately 3 Myr. Evidently, the present rate of shortening is a few times higher than the average rate over 20 Myr.

Although shallow deformations of the Tien Shan have been fairly well studied [Makarov, 1977], its deep structure is known much worse. Seismic data show that wave velocities in the crust and upper mantle of the Tien Shan east of the Talas-Fergana fault are lower than to the west of the fault [Vinnik et al., 1983; Roecker et al., 1993]; however, the resolution of these data is limited by the amount and quality of records on photographic paper. The Moho depth varies within a range of about 25 km [Roecker, 2001]. The local earthquake tomography points to a strong lateral heterogeneity of the crust [Ghose et al., 1998]. A lower velocity fractured layer of a varying thickness was detected in the upper crust [Vinnik et al., 2002b]. Seismic heterogeneities of the crust correlate with electrical conductivity variations [Trapeznikov et al., 1997]. Seismic data point to an azimuthal anisotropy of the Tien Shan upper mantle associated with an ordered orientation of olivine crystals. The anisotropy varies with depth [Vinnik, 2002a] and laterally [Makeyeva et al., 1992; Wolfe and Vernon, 1998].

More comprehensive investigations of the Tien Shan deep structure became possible when a few tens of broadband digital seismic stations were installed in this region (Fig. 1). Digital data were used for studying the crust and mantle with the use of *P* and *S* receiver functions [Kosarev et al., 1993; Chen et al., 1997;
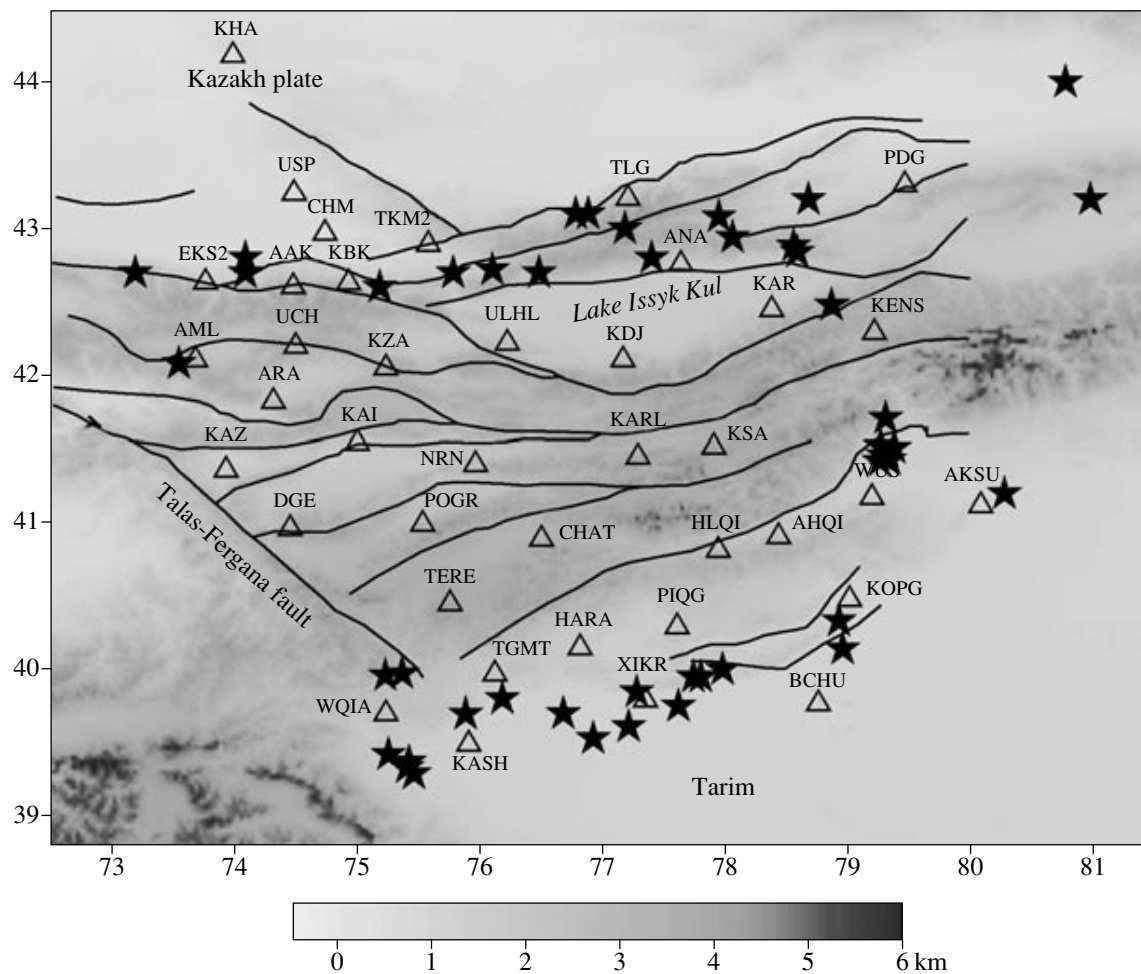
Fig. 1. Map of the region including seismic stations (triangles) and epicenters of large ($M > 5.8$) earthquakes (stars). The lines are active faults [Ghose et al., 1998]. Earthquakes before 1978 are taken from the catalog in [Kondorskaya and Shebalin, 1982].

Roecker, 2001; Oreshin et al., 2002; Vinnik et al., 2002b, 2004]. The technique of *P* receiver functions [Vinnik, 1977; Langston, 1979] is well-known and widely used throughout the world. This method mainly employs *Ps* waves converted from *P* to *S* at seismic boundaries near a seismic station. The technique of *S* receiver functions employing *Sp* converted waves has been proposed recently [Farra and Vinnik, 2000] and used by various authors [Vinnik et al., 2001; Vinnik and Farra, 2002; Oreshin et al., 2002]. The *S* receiver functions have revealed beneath some stations a high velocity mantle lid (seismic mantle lithosphere) and an underlying low velocity layer (seismic asthenosphere) [Oreshin et al., 2002].

Notwithstanding the progress in seismic observations and methods of their analysis, the problem of constructing a 3-D velocity model of the Tien Shan crust and upper mantle with a resolution adequate for tectonic applications has been solved, at best, only par-

tially. In regional studies of the lithosphere, the highest resolution is attained in the classical method of seismic tomography using anomalies (residuals) of traveltimes of *P* or *S* waves from distant earthquakes [Aki et al., 1977]. However, depth resolution of this method is negligible in an upper layer whose thickness depends on the density of the network of seismic stations. With an average distance between stations of about 100 km (Fig. 1), the upper layer thickness is estimated at about the same value (about 100 km). Thus, the lithosphere, i.e., the layer of most interest for tectonic applications, is virtually excluded from studies.

In this work, we use a method of constructing a 3-D velocity model from the Earth's surface to a depth of 200–300 km. The idea is a combined use of teleseismic anomalies of *P* and *S* wave traveltimes and the corresponding receiver functions. This method develops the previously described technique used for the joint inver-

sion of P and S receiver functions, which is called receiver function tomography [Vinnik et al., 2004].

The joint inversion of receiver functions of the two types is advantageous for the following reasons. The interference of waves converted by deep boundaries and waves multiply reflected or scattered from shallow heterogeneities is a drawback of the method of P receiver functions. An advantage of S receiver functions is that, in this method, multiples from crustal boundaries are recorded later than the waves converted by boundaries in the upper mantle. On the other hand, the P receiver functions are more suitable for the study of the upper crust. Moreover, converted waves of the two types at the same epicentral distances sound the medium at different angles.

However, the velocity model obtained by joint inversion of receiver functions of the two types is not the only possible model, and additional data must be used for reducing the ambiguity. The velocity model predicts traveltime residuals of waves from distant earthquakes relative to the standard times. The traveltime residual is determined by the average velocity, and the receiver functions are sensitive to velocity variations with depth and, to a lesser degree, to absolute velocity values. Therefore, the joint inversion of receiver functions and independently measured traveltime residuals of P and S waves at each station can provide a more reliable model.

The paper has the following structure. The technique of joint inversion of P and S receiver functions is briefly described in the second section, following [Vinnik et al., 2004]. The joint inversion of receiver functions and traveltime residuals is described in the third section, where results of the joint inversion of records of Tien Shan seismic stations are also presented. These results are discussed in the last section.

2. JOINT INVERSION OF RECEIVER FUNCTIONS

A receiver function is the response of the medium near a seismic station to a disturbance produced by P or S waves from far earthquakes. To identify this response against the noise background, records of a few tens of earthquakes at one station are processed jointly. This requires the elimination of distinctions between individual records due to distinctions in source processes. The wave radiated by an earthquake can be represented as a convolution of the standard bell-shaped pulse and an individual source function. The standard pulse is reconstructed by the projection of a P or S wave record onto the principal direction of its displacements in the wave propagation plane and deconvolution in the time domain with adequate regularization.

The converted waves form the component of a seismogram orthogonal to the principal component in the same plane. The filtering of this component with the same deconvolution filter equalizes secondary waves. The equalized second component is normalized through its division by the maximum value of the first component. Further, the equalized components are stacked for the noise suppression. The stacking result is called the receiver function. In the general case, waves converted by deep boundaries differ in slowness from the primary wave and, to identify them, individual receiver functions are stacked with shifts. However, this is not done in our work because the effect of the shifts can be neglected in the study ranges of depths and wave periods. Further, the main and the second components are denoted, respectively, as L and Q (for P receiver functions) or as Q and L (for S receiver functions). Some details that can be found in other papers are omitted in this brief description.

As in other similar studies of the receiver function inversion, it is assumed that the medium in the vicinity of a seismic station is isotropic and horizontally layered. The lateral heterogeneity of the medium is described as a mosaic of individual homogeneous blocks. A trial model for a single block is described by the velocities V_P and V_S of P and S waves, the density ρ, and the thickness of each plane layer. In the modeling of receiver functions, the synthetic Q and L components (for the respective P and S receiver functions)

$$Q_{P,\,syn}(t, \mathbf{m}, c_P) = \frac{1}{2\pi} \int_{-\infty}^{\infty} \frac{H_{P,\,Q}(\omega, \mathbf{m}, c_P)}{H_{P,\,L}(\omega, \mathbf{m}, c_P)} \quad (1)$$
$$\times L_{P,\,obs}(\omega) \exp(i\omega t)\, d\omega,$$

$$L_{SV,\,syn}(t, \mathbf{m}, c_{SV}) = \frac{1}{2\pi} \int_{-\infty}^{\infty} \frac{H_{SV,\,L}(\omega, \mathbf{m}, c_{SV})}{H_{SV,\,Q}(\omega, \mathbf{m}, c_{SV})} \quad (2)$$
$$\times Q_{SV,\,obs}(\omega) \exp(i\omega t)\, d\omega$$

are calculated for each trial model. Here, t is time, ω is the angular frequency, $\mathbf{m}$ is the vector of unknown parameters of the model, c_P and c_{SV} are the apparent velocities, the subscripts "obs" and "syn" refer to actual receiver functions and their synthetic analogues, and H are the theoretical transfer functions [Haskell, 1962] for a stack of layers.

The cost function E is calculated for each trial model:

$$E(\mathbf{m}) = (1 - \alpha) \| Q_{P,\,obs}(t) - Q_{P,\,syn}(t, \mathbf{m}, c_P) \|$$
$$+ \alpha \| L_{SV,\,obs}(t) - L_{SV,\,syn}(t, \mathbf{m}, c_{SV}) \|, \quad (3)$$

where α determines the relative weights of receiver functions of different types. In practice, the value of α is close to 0.5. The optimal model minimizes E.

The optimal model is sought by the adaptive simulating annealing algorithm [Ingber, 1989]. Models constructed with the use of gradient methods of the type described in [Kosarev et al., 1993] can depend on the initial model because the error surface can have a few or many local minimums. As distinct from the gradient methods, the algorithm applied here seeks the global
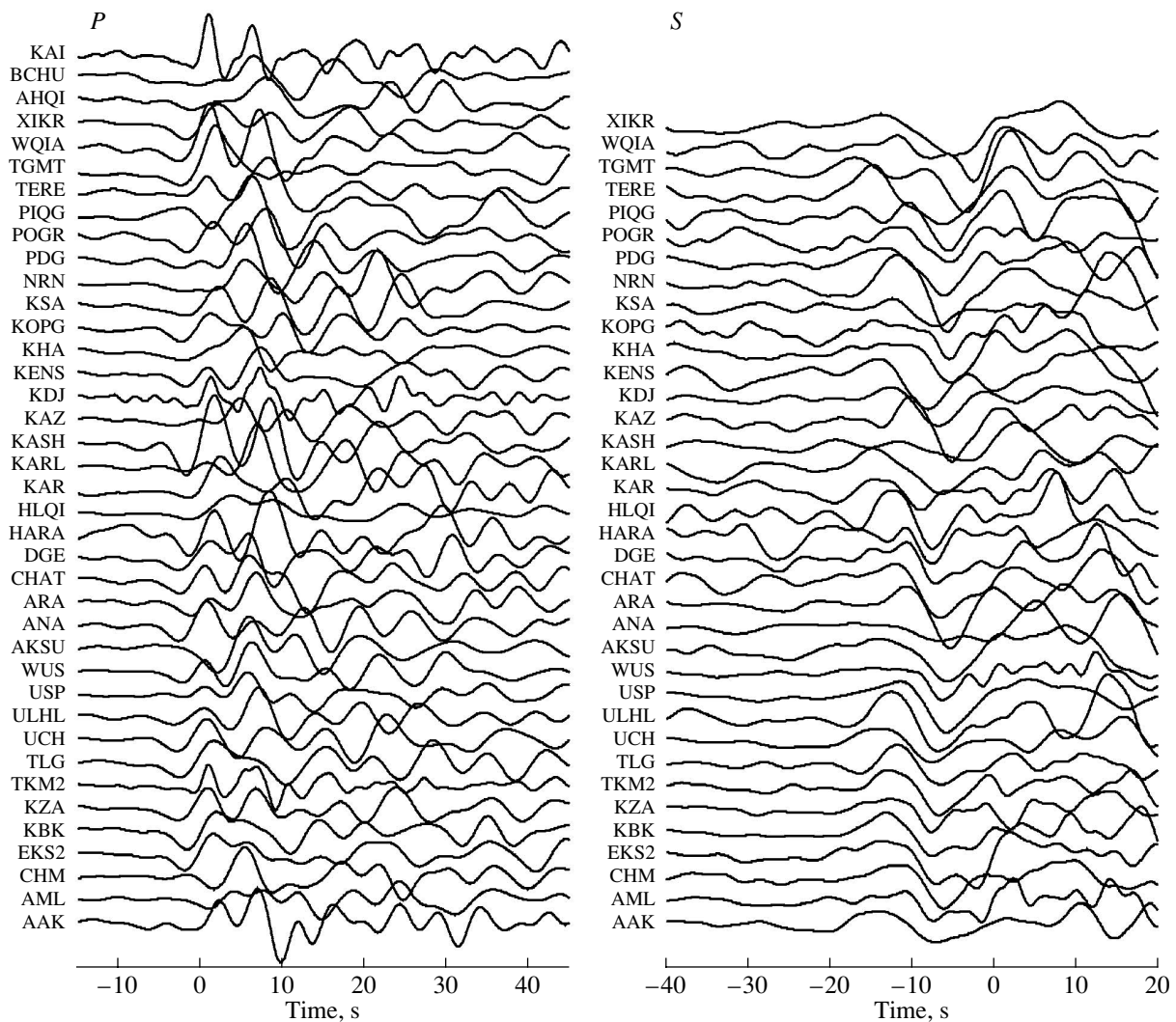
Fig. 2. *Q* component of stacked *P* receiver functions (to the left) and *L* component of *S* receiver functions (to the right). The origin of the time scale is the arrival of *P* (to the left) and *S* (to the right) wave. The supposed arrivals of the *Sp* phase from the Moho are marked by dots.

minimum and belongs to the group of methods close to the Monte Carlo approach but scans the space of possible solutions more effectively than the classical Monte Carlo method.

3. JOINT INVERSION OF RECEIVER FUNCTIONS AND TRAVELTIME RESIDUALS FROM DATA OF TIEN SHAN STATIONS

Digital seismic stations of the central Tien Shan belong to the KNET (9 stations in the northwest of the region), GSN/IRIS (the AAK and TLG stations), Geoscope (the WUS station), and GHENGIS (28 stations) networks [Roecker, 2001]. The latter network was in operation for about a year and a half; the remaining stations operated during periods of a few years to ten years or more. The receiver functions are determined for

earthquakes in an azimuthal sector of 90° to 120°. This sector is very rich in earthquakes in a wide range of epicentral distances. The majority of receiver functions have been obtained previously [Vinnik and Farra, 2002; Vinnik et al., 2002b; Oreshin et al., 2002].

The *P* receiver functions (Fig. 2) are obtained in the epicentral interval from 40° to 100°. Generally, the number of individual functions for one station amounts to a few tens. Seismograms with periods of 1–2 s contain random noise due to scattering by small-scale heterogeneities. To weaken this noise, periods shorter than 5 s are suppressed by low-pass filtering. The *Ps* phases from the Moho are represented by pulses of positive polarity at a time of 6–8 s. At some stations, such a pulse is preceded by another pulse at a time of 1–3 s, which is the *Ps* wave formed at the base of the low velocity fractured layer or, in the case of stations in

China, at the base of loose sediments. Functions in the time interval from –5 to +12 s were generally used in modeling.

The *S* receiver functions (Fig. 2) are obtained in the epicentral range from 65° to more than 100°. Their predominant period is about 10 s. The average number of individual receiver functions ranges from about 25 for stations of the GHENGIS network to 70–90 for long-term stations. For several GHENGIS stations, the amount and quality of records were insufficient for the reliable determination of *S* receiver functions. In Fig. 2, the *Sp* wave converted by the Moho is identified as a pulse of negative polarity a few seconds ahead of the zero time. Another phase of a comparable amplitude and positive polarity is often observed at a time of about –14 s (the AAK, KBK, TKM2, TLG, UCH, ULHL, HLQI, KAZ, NRN, and TERE stations). This phase can be formed at a negative seismic boundary (with a velocity drop; in this case, the top of the seismic asthenosphere); however, this cannot be stated only from the form of the receiver function. The functions in the time interval from –30 to 0 s were used in modeling.

To estimate the *P* and *S* traveltime residuals, we used records of ten earthquakes in the same azimuthal sector, where the receiver functions were obtained, with distinct arrivals well recorded at the majority of stations. To eliminate possible effects associated with distinctions in the frequency responses of stations belonging to different networks, we performed the reconstruction of ground motions; however, these effects were found to be actually small. Distinct arrivals were traced from station to station, and their deviations from the time at the TLG station were calculated. The traveltime differences determined by distinctions in epicentral distances were eliminated from these deviations. The IASP91 standard traveltime curves were used in this case [Kennett and Engdahl, 1991].

The resulting traveltime residuals are relative, i.e., they are determined with respect to the reference station. However, our technique requires absolute traveltime anomalies determined with respect to the IASP91 standard velocity structure. In the general case, the absolute residual can be determined from exact values of the epicentral distance, hypocentral depth, and source time of each earthquake, which is, naturally, impossible. Therefore, we used a different approach based on the fact that, in the majority of regions of the world, the top and base of the mantle transition zone occur virtually at the same depths (410 and 660 km, respectively [Chevrot et al., 1999]). A substantial topography of the transition zone boundaries has been established only in subduction zones and at some of the largest hotspots; however, the Tien Shan region does not belong to such regions.

Another important circumstance is that traveltime residuals usually form mostly in the upper, approximately 250-km-thick layer of the Earth. This fact has been established from numerous observations of long
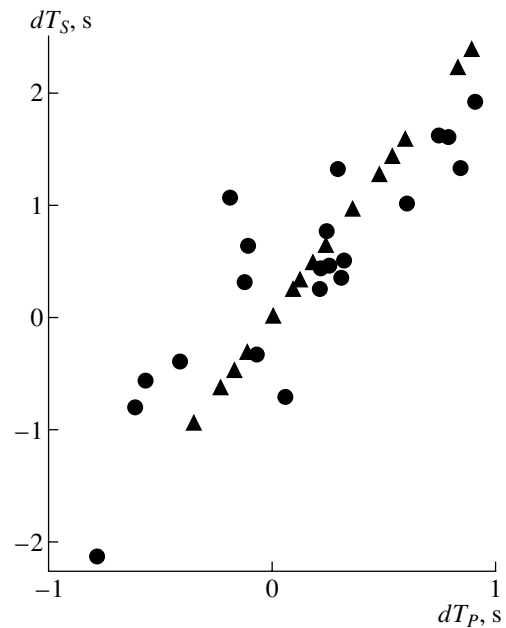

Fig. 3. Relative (circles) and absolute (triangles) traveltime residuals of teleseismic *P* and *S* waves at 21 stations of the Tien Shan. The relative residuals are determined with respect to the TLG station with the aid of the IASP91 traveltime curves. The method for the determination of absolute residuals is described in the text.

period surface waves. The peak-to-valley values of lateral variations in the *S* wave velocity in this layer attain 20% and are controlled by high velocity roots of ancient platforms in some regions and by low velocities of the asthenosphere in other regions. Both features are established with certainty at depths that typically do not exceed 200–250 km. Subduction zones and a few of the largest mantle plumes are also exceptions; however, as mentioned above, the Tien Shan is not among these.

Following [Vinnik et al., 1999] and taking into account the above considerations, the arrival time anomaly dT_{Ps} (deviation from the standard time) of the *Ps* wave from one of the transition zone boundaries can be written as

$$dT_{Ps} = dT_S - dT_P,$$

where dT_S and dT_P are the absolute teleseismic traveltime residuals of *S* and *P* waves. This relation is a natural consequence of the fact that the arrival time of the converted wave is measured from the arrival time of the primary wave, in this case, the *P* wave. This relation can be rewritten as $dT_{Ps} = (k - 1)dT_P$, where *k* is the known ratio of absolute residuals. The expressions for the absolute residuals

$$dT_P = dT_{Ps}/(k - 1); \quad dT_S = dT_{Ps}(1 + 1/(k - 1))$$

follow from this relation.

Waves converted by boundaries in the transition zone were identified at approximately half of the sta-
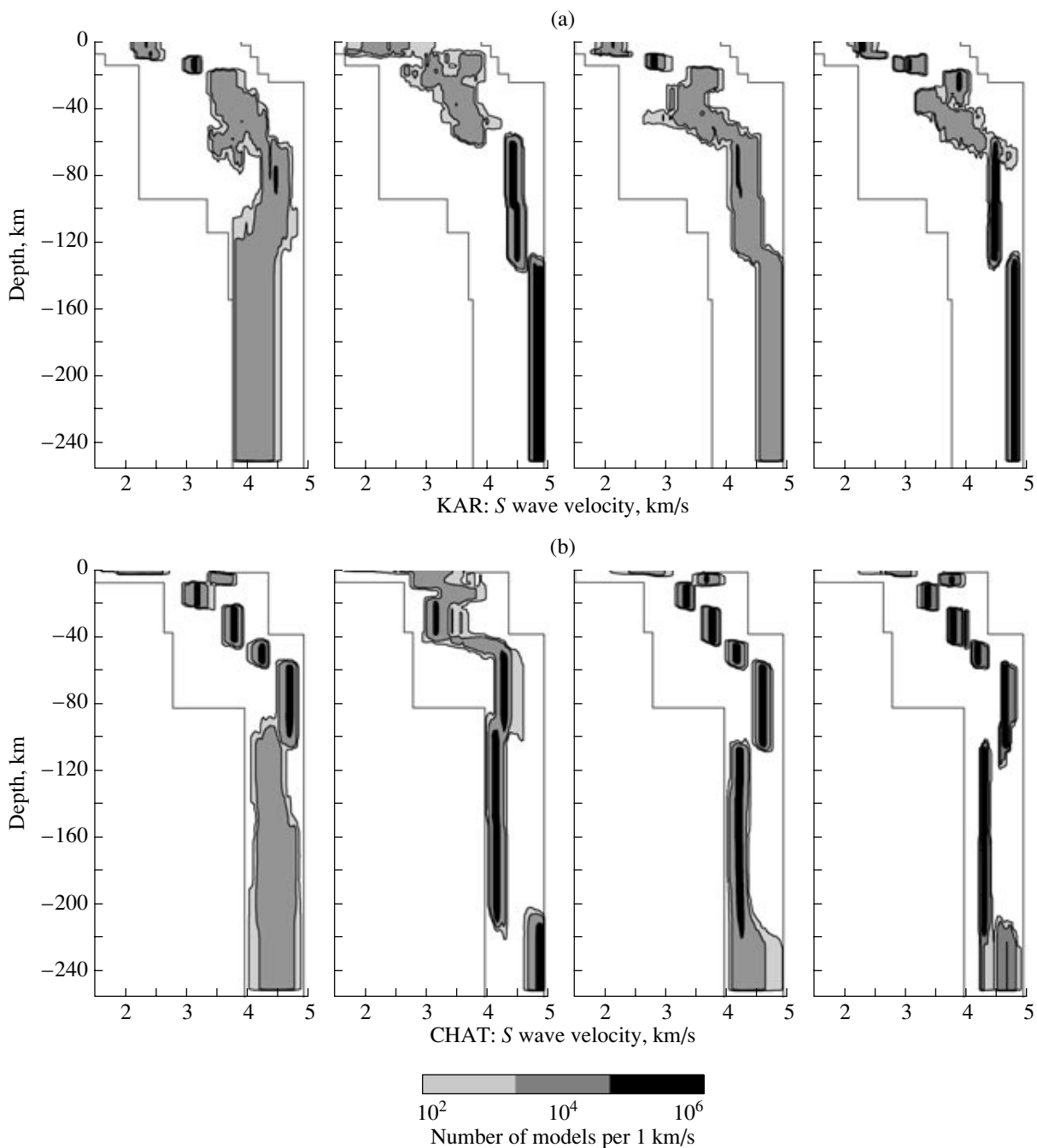
Fig. 4. Examples of the marginal a posteriori distributions of *S* wave velocity structures obtained (from left to right) by the separate inversions of *P* and *S* receiver functions, by joint inversion of *P* and *S* receiver functions, and by the joint inversion of receiver functions and absolute traveltime residuals for the KAR (a) and CHAT (b) stations. The boundaries of the a priori *S* velocity distribution are shown.

tions. With the standard value $k = 2.7$, the absolute residuals are, on average, close to relative residuals at the same stations (Fig. 3), and below we equate relative and absolute anomalies.

In the actual inversion of the data described above, the model is described by a group of layers whose thicknesses, along with the *P* and *S* velocities, are

included in **m**. The number of layers usually does not exceed seven to nine. At depths greater than 250 km, the wave velocities coincide with the IASP91 standard values. The angles i_P and i_{SV} are known for individual receiver functions but not for the stacked functions. Therefore, they are treated unknowns to be found in the vicinity of average values. As regards the density, it is

supposed to obey the Birch law. The apparent velocity of *P* waves is determined as the average of individual values and is generally about 17 km/s. In the wave packet of transverse waves, the phase *S* prevails at distances of less than 90°, and the phase *SKS* with an apparent velocity higher than that of *S* prevails at greater distances. Numerical modeling shows that the contribution of *SKS* to the total amplitude of waves converted by shallow boundaries is negligible, and the average apparent velocity of the *S* phase (usually about 10 km/s) is used in calculations. A 3-D model is constructed through the interpolation of station models [Vinnik et al., 2004].

The effect of the combination of receiver functions and traveltime residuals is demonstrated by examples of the marginal a posteriori distribution of V_S cross sections (Fig. 4). The a posteriori probability distribution in the space of models is formulated, for example, in [Mosegaard and Sambridge, 2002]. In the Bayes approach to the solution of inverse problems, the a posteriori distribution of the probability $f(\mathbf{m})$ is given by the formula

$$f(\mathbf{m}) = C_f L(\mathbf{m})\rho(\mathbf{m}),$$

where C_f is the normalization constant, $L(\mathbf{m})$ is the likelihood function, and $\rho(\mathbf{m})$ is the a priori probability distribution. The function $L(\mathbf{m})$ has the form

$$L(\mathbf{m}) = C_L \exp(-E(\mathbf{m})),$$

where C_L is a constant and $E(\mathbf{m})$ is the cost function representing the deviations of observational data from the calculated data of the model $\mathbf{m}$.

The a priori distribution was assumed to be uniform in each parameter in the interval specified for this parameter. To obtain a sample of models with an a posteriori distribution of the probability density, we used the algorithm proposed in [Metropolis et al., 1953]. Algorithms of this type allow one to avoid the search for models in regions of a low probability density, thereby strongly decreasing the time of computations.

The cascade variant of the Metropolis algorithm applied in our work is well adapted for a combination of various groups of data and makes it possible to examine the influence of additional data on the inversion results. The velocity distribution in the crust of the KAR station (Fig. 4a) is a very wide for the separate inversion of receiver functions, but becomes narrower for the joint inversion. Finally, the joint inversion of receiver functions and traveltime residuals is very narrow in both the crust and the mantle. The Moho at a depth between 50 and 60 km, the positive boundary at a depth of 130 km, and the low velocity layer in the crust at a depth of 40–50 km are well resolved. Advantages of the joint inversion are also seen from the example of the CHAT station. The Moho at a depth of about 60 km, the low velocity layer in the crust at a depth of 20 km, and the well-expressed low velocity layer in the mantle with the top at a depth of about 100 km are well resolved in the models obtained in this work.

The resulting 3-D model of the *S* wave velocity in the crust is presented in the horizontal cross section in Fig. 5 and the vertical cross section in Fig. 6. The mantle is presented by the horizontal cross sections at two depths (Fig. 7).

The Moho topography (Fig. 5b) is shown under the assumption that *S* wave velocities exceeding 4.2 km/s characterize the mantle. At a few stations, the crust–mantle transition was found to be diffuse and the Moho depth was not determined.

4. DISCUSSION

Our estimate of the V_S uncertainty in the resulting model is, on average, about 0.1 km/s. Large-scale heterogeneities established from data of several stations are the most reliable. The low velocity anomaly at depths of 10–35 km in the central Tien Shan is such a heterogeneity in the crust (Fig. 5a). The *S* wave velocity within this anomaly is lower than in the adjacent areas by up to 10%. The reality of this anomaly is confirmed by comparison with independent estimates. In particular, at a qualitative level, our result does not contradict the data presented in [Roecker et al., 1993]. An abrupt transition from low velocities in the upper and middle crust under the mountainous structure to high velocities in the piedmont area was previously revealed by studies in the northern Tien Shan near the AAK station [Ghose et al., 1998; Vinnik et al., 2002b].

In the upper mantle at depths of 70–90 km, our analysis identified two low velocity anomalies: in the northwest and in the southeast (Fig. 7a). The NW anomaly corresponds to small-volume outflows of basalts of Late Cretaceous–Early Paleogene age [Dobretsov and Zagruzina, 1977; Knauf et al., 1980]. In the Tien Shan, there is no reliable evidence of rifting at that time and magma is similar in composition to basalts of oceanic islands [Grachev, 1999; Sobel and Arnaud, 2000]. This similarity suggests the presence of a small plume in the upper mantle of the Tien Shan. The correspondence of the anomaly at depths of 70–90 km to its manifestations at the Earth's surface indicates the absence of a considerable (exceeding 20–30 km) displacement of the crust relative to the underlying mantle over the past 50 Myr. A somewhat larger displacement is possible only in the southernmost regions, where the position of basalts is at variance with the low velocities.

The SE low velocity anomaly can be of the same origin. The surface manifestation of this anomaly is the Bachu uplift (the Tarim region) in the area of the BCHU seismic station (Fig. 1). The uplift is characterized by a reduced (to about 1 km) thickness of Cenozoic sediments, which are usually 8–9 km thick [Li et al., 1996]. Outflows of basalts in this area could have been prevented by an early onset of the compression regime in the crust.

At depths of 110–130 km (Fig. 7b), the coherent low velocity anomaly is elongated in the direction perpendicular to the main ranges of the Tien Shan. This con-
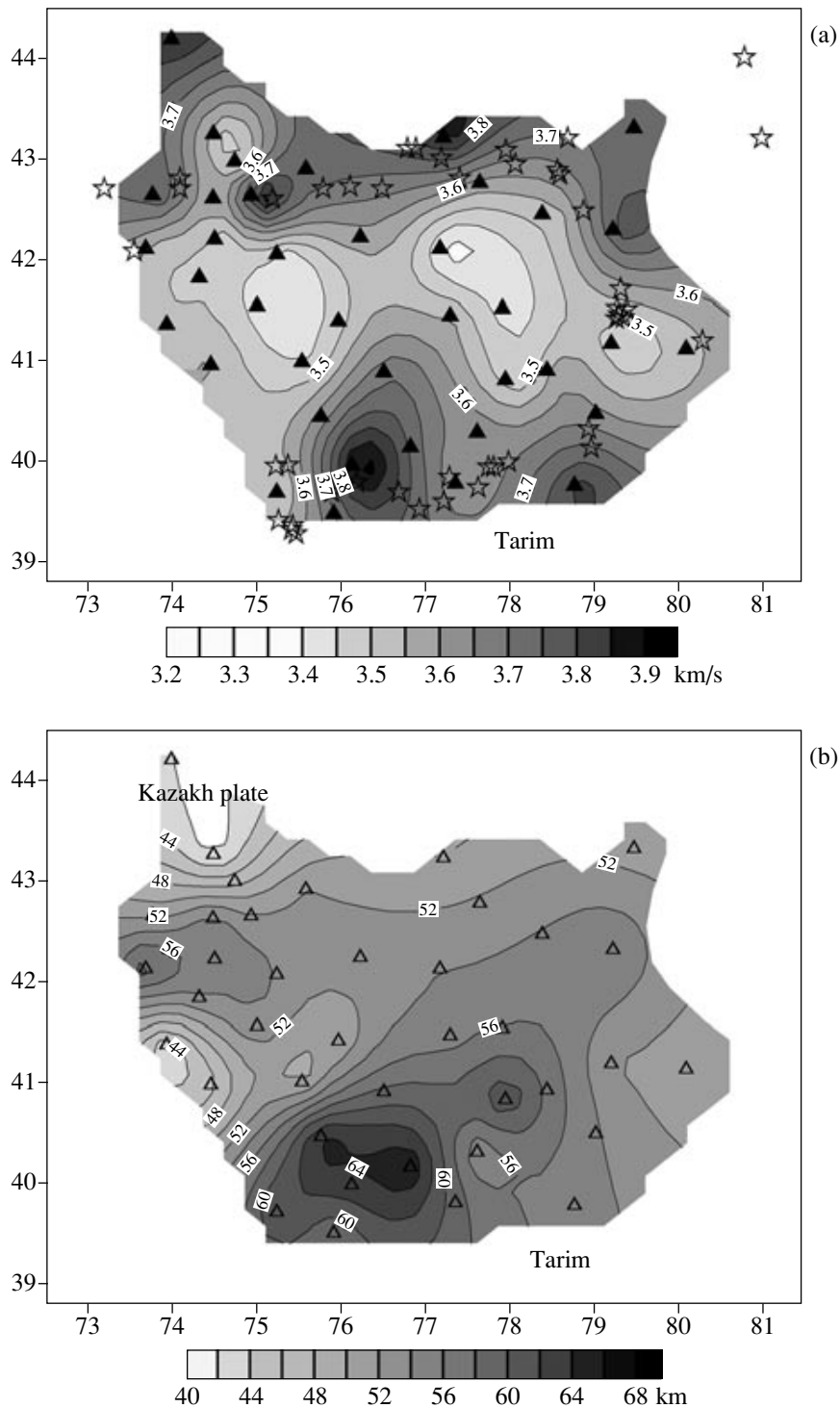
Fig. 5. *S* wave velocity averaged in the 10–35-km interval (a) and the crustal thickness (b). Seismic stations and epicenters of large earthquakes are shown, as in Fig. 1, by triangles and stars.

figuration can be due to the effect of mantle extension along the Tien Shan strike and its compression in the perpendicular direction. Some rifts, for example, the Rhine graben, have formed in a similar way in a compression environment [Sengor et al., 1978].

A well-expressed high velocity anomaly centered at (41°N, 75°E) corresponds to the Naryn depression and its interpretation as a fragment of an ancient platform [Krestnikov and Nersesov, 1962]. A high velocity body in the area (42.6°N, 75.3°E) corresponds to the Chu
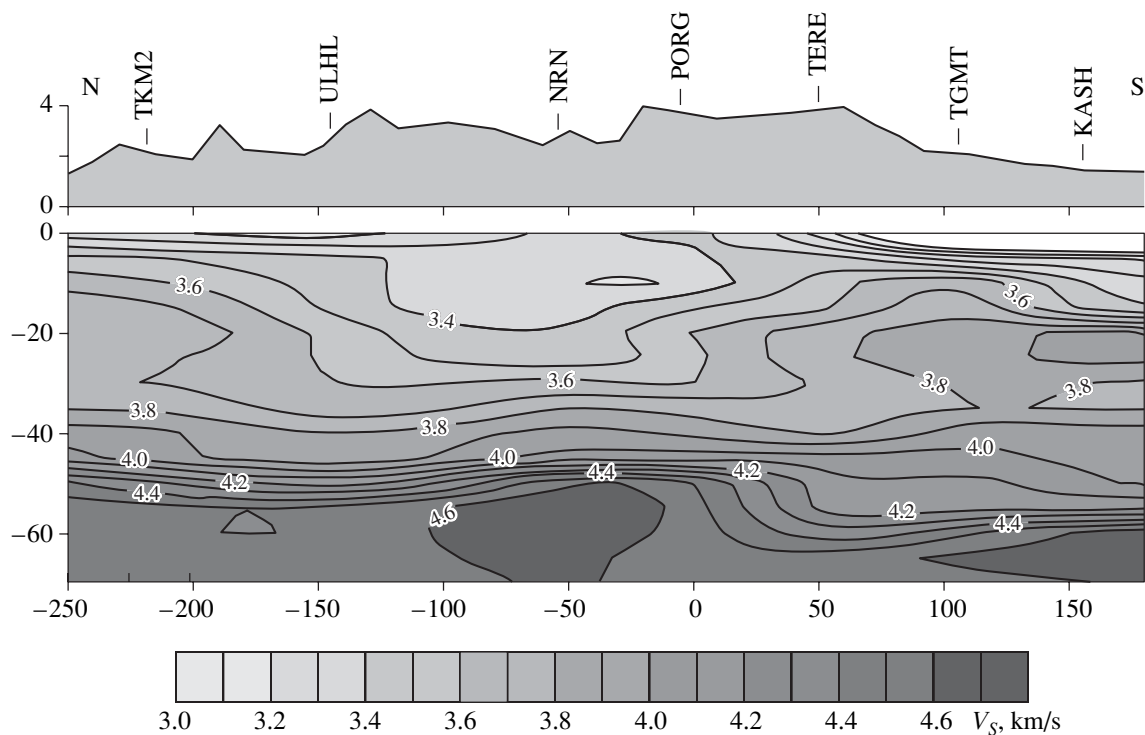
Fig. 6. *S* wave velocity structure on a profile along 76°E. The crust–mantle boundary approximately corresponds to a velocity of 4.2 km/s.

depression. The eastern, deepest part of the Issyk Kul depression overlies a large high-velocity body centered at (41.5°N, 77.3°E). Thus, some depressions of the Tien Shan are controlled by heterogeneities of the mantle lithosphere.

Large (*M* > 5.8) earthquakes of the Tien Shan are distinguished by the following regular pattern: such earthquakes have not occurred in the central Tien Shan over the period covered by instrumental or historical observations (Fig. 1), notwithstanding the presence of active faults in this region and high seismicity of its margins. In contrast to large earthquakes, the distribution of weak earthquakes over the surface is diffuse. The regular pattern of the surface distribution of Tien Shan large earthquakes has long been known [Makarov, 1977] but has not been clearly explained. Previously, one might have supposed that the present crustal deformations of the Tien Shan at its margins are substantially larger than in its central part; however, this idea contradicts both data of cosmic geodesy [Abdrakhmatov et al., 1996; Reigber et al., 2001] and recent geological evidence. The long-term absence of strong earthquakes in the presence of large deformations could mean the accumulation of crustal stresses capable of releasing in a series of catastrophic earthquakes in the future; however, our data suggest a different interpretation.

The low velocity zone in the middle crust (Fig. 5) evidently coincides with the region of absent large earthquakes. This coincidence gives grounds for two conclusions: (1) the rheology of the middle crust has an influence on the occurrence of large earthquakes, and (2) the crust of the low velocity zone is mechanically too weak to accumulate the elastic energy necessary for large earthquakes. The low seismic velocity and the mechanical weakness can be caused by the presence of water. The mechanical behavior of the upper crust is governed by stick-slip motions, whereas plastic deformations prevail at larger depths [Kohlstedt et al., 1995]. The mechanical weakness of a wet rock is due to a high pore pressure and chemical processes [Kirbi, 1983; Kohlstedt et al., 1995]. Water decreases the solidus of rocks by about a few hundred degrees, which can lead to their melting at a relatively low temperature [Kadik et al., 1971], and the transition from brittle failure to plastic flow can occur at a small depth. The same phenomena reduce the velocity of transverse waves. Water and especially brine reduce the electric resistivity of rocks. The fact that the resistivity in the middle crust of the Tien Shan is lower compared with the neighboring platform in the north has been documented by magnetotelluric soundings [Trapeznikov et al., 1997].

The origin of water in the Tien Shan crust is attributed to the dehydration of amphibolites in the lower crust due to a recent (10–20 Ma) temperature increase [Trapeznikov et al., 1997]. However, practically the only reliable change in the thermal field of the Tien Shan during the Cenozoic is a small plume in the Early
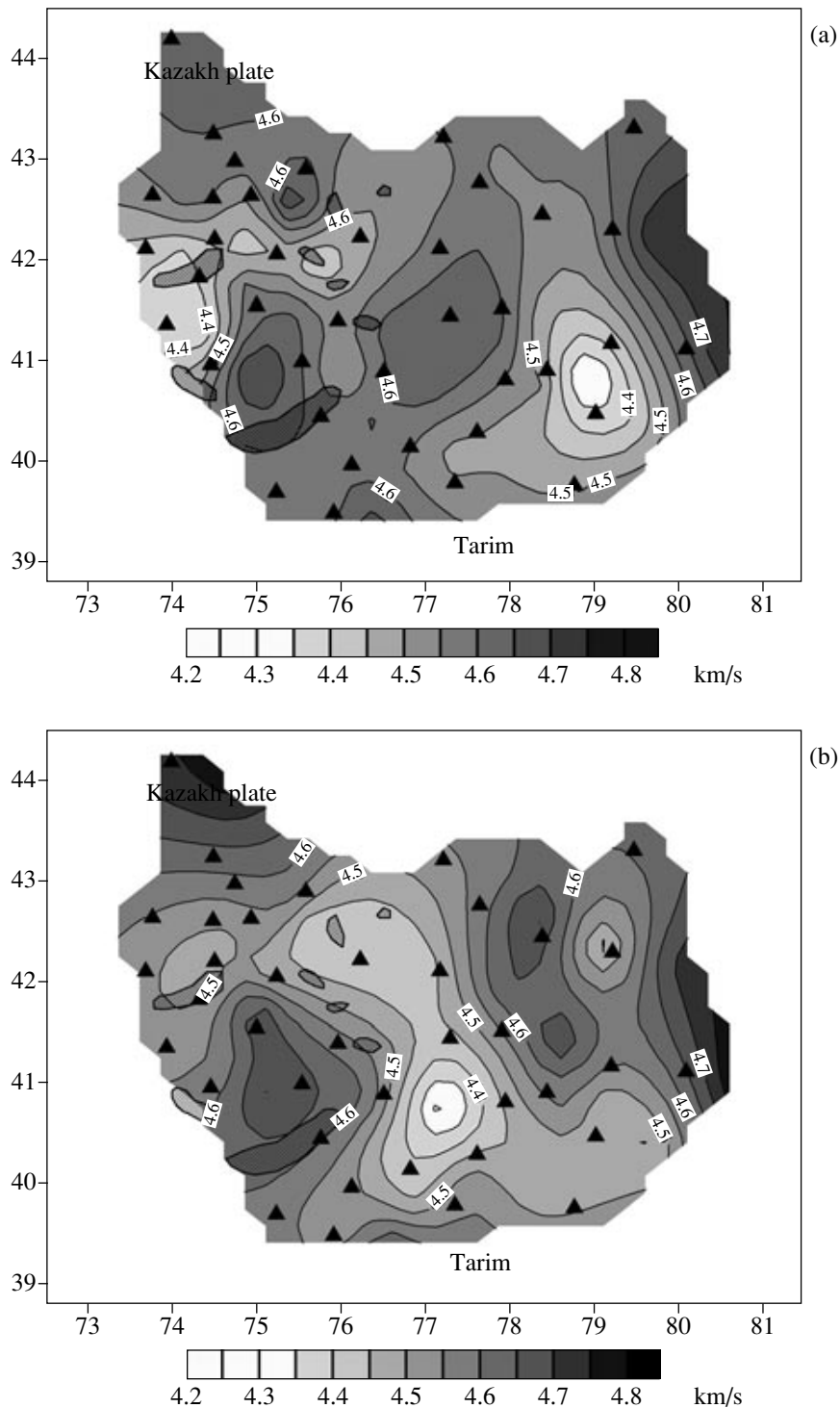
Fig. 7. Average velocity of *S* waves at depths of 70–90 km (a) and 110–130 km (b). Basaltic flows of the Upper Cretaceous–Early Paleogene are cross-hatched. Seismic stations are shown by triangles.

Paleogene (about 55 Ma). The low velocity anomalies in the upper mantle might be remnants of this plume. The temperature in the crust can increase due to delamination of the subcrustal lithosphere [Bird, 1978]

because, in this case, the crust comes into direct contact with hot rocks of the asthenosphere. Low velocity anomalies in the upper layer of the mantle result from the delamination. If the low velocity anomalies in the
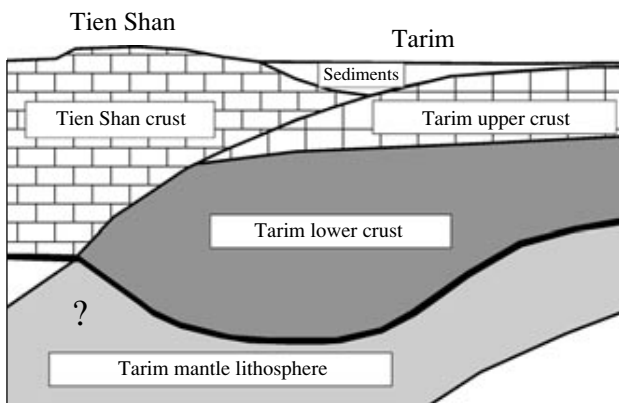
Fig. 8. Schematic illustration of the lower crust accumulation through the underthrusting of the Tien Shan by the Tarim lithosphere.

crust and upper mantle of the Tien Shan were directly related, the geographic outlines of the anomalies would be similar; however, Figs. 5 and 7 give no grounds for such an inference. No clear correlation exists between the velocity anomalies in the crust in Fig. 5 and the temperature anomalies [Duchkov et al., 2001]; however, one should take into account that the thermal field of the Tien Shan has been studied insufficiently. If the low velocity and mechanical weakness of the Tien Shan crust are due, at least in part, to the young orogenesis, one may suggest that the conductive heat transfer is replaced in part by convective jet transport, which led to a temperature increase in the process of orogenesis.

As an alternative to the recent heating, one may suggest that the fluids and mechanical weakness of the crust have been inherited from the Paleozoic Tien Shan. In the general case, the continental lithosphere contains two high strength layers: (1) the upper crust and (2) the upper mantle at depths of up to 70 km [Kirbi, 1983]. If at least one of these layers is weakened, deformations can be localized in a weak zone. The idea of a weak lithosphere of the Tien Shan was used in preceding works. If the Tien Shan is modeled as a result of the convergence of two lithospheric plates, the flexural rigidity of the southern (Tarim) plate must be much greater than the flexural rigidity of the northern plate [Burov et al., 1990]. The formation of the Tien Shan under the action of compressive stresses can be attributed to the weakness of the mantle lithosphere of the Tien Shan as compared with the rigid Tarim block [Neil and Houseman, 1997].

The velocity structure of the crust (Fig. 6) calls for a special discussion. Here, in the Tarim–Tien Shan contact zone, the crust is thickest (about 60 km). The crust–mantle boundary sinks in a ~20-km jump due to an increase in the thickness of the lower crust (with an S wave velocity of 3.8–4 km/s). According to DSS data, a similar phenomenon is observed in the south of the Tarim region, in the area of its underthrusting beneath

the Kunlun [Li et al., 2002]. Various studies, for example, [Scharer et al., 2004], present facts indicating that Tarim is thrust under the Tien Shan, and an increase in the lower crust thickness at the Tarim margins is likely associated with this process. In the underthrusting zone, the mechanically weak lower crust of Tarim exfoliates and accumulates in approximately the same way as an accretionary prism during subduction of the oceanic lithosphere (Fig. 8). The exfoliation and accumulation of rocks of the lower crust in the underthrusting zone qualitatively agrees with the results of thermomechanical modeling [Touissaint et al., 2004].

REFERENCES

1. K. Ye. Abdrakhmatov, S. A. Aldazhanov, B. H. Hager, et al., "Relatively Recent Construction of the Tien Shan Inferred from GPS Measurements of Present-Day Crustal Deformation Rates," Nature **384**, 450–453 (1996).

2. K. E. Abdrakhmatov, R. Weldon, S. Thompson, et al., "The Origin, Direction, and Rate of Recent Compression of the Central Tien Shan (Kyrgyzstan)," Geol. Geofiz. **42** (10), 1585–1609 (2001).

3. K. Aki, A. Christofferson, and E. S. Husebye, "Determination of the Three-Dimensional Seismic Structure of the Lithosphere," J. Geophys. Res. **82** (2), 277–296 (1977).

4. P. Bird, "Initiation of Intracontinental Subduction in Himalaya," J. Geoph. Res. **83**, 4975–4987 (1978).

5. E. V. Burov, M. Kogan, Lyon-Caen, and P. Molnar, "Gravity Anomalies for Deep Structure, and Dynamic Processes beneath the Tien Shan," Earth Planet. Sci. Lett. **96**, 367–383 (1990).

6. V. S. Burtman, "Structural Geology of Variscan Tien Shan," Am. J. Sci. **275**, 157–186 (1975).

7. Y. H. Chen, S. W. Roecker, and G. Kosarev, "Elevation of the 410 km Discontinuity beneath the Central Tien Shan: Evidence for a Detached Lithospheric Root," Geophys. Res. Lett. **24** (12), 1531–1534 (1997).

8. S. Chevrot, L. Vinnik, and J.-P. Montagner, "Global-Scale Analysis of the Mantle *Pds* Phases," J. Geophys. Res. **104** (B9), 20 203–20 219 (1999).

9. G. I. Dobretsov and I. A. Zagruzina, "Young Basaltoid Magmatic Activity in the Eastern Tien Shan," Dokl. Akad. Nauk SSSR **235**, 67–70 (1977).

10. A. D. Duchkov, Yu. G. Shvartsman, and L. S. Sokolova, "Deep Heat Flow in the Tien Shan: Achievements and Problems," Geol. Geofiz. **42** (10), 1516–1531 (2001).

11. V. Farra and L. Vinnik, "Upper Mantle Stratification by *P* and *S* Receiver Functions," Geophys. J. Int. **141** (3), 699–712 (2000).

12. S. Ghose, M. Hamburger, and J. Virieux, "Three-Dimensional Velocity Structure and Earthquake Locations beneath the Northern Tien Shan of Kyrgyzstan, Central Asia," J. Geophys. Res. **103** (B2), 2725–2748 (1998).

13. A. F. Grachev, "Early Cenozoic Magmatism and Geodynamics of North Tien Shan," Izvestiya, Phys. Solid Earth **35** (10), 815–839 (1999).

14. N. A. Haskell, "Crustal Reflection of Plane *P* and *SV* Waves," J. Geophys. Res. **67**, 4751–4767 (1962).

15. L. Ingber, "Very Fast Simulated Annealing," Math. Comput. Model. **12**, 967–993, (1989).

16. A. A. Kadik, E. B. Lebedev, and N. I. Khitarov, *Water in Magmatic Melts* (Nauka, Moscow, 1971) [in Russian].

17. B. L. N. Kennett and E. R. Engdahl, "Traveltimes for Global Earthquake Location and Phase Identification," Geophys. J. Int. **105**, 429–465 (1991).

18. S. H. Kirbi, "Rheology of the Lithosphere," Rev. Geophys. Space Phys. **21** (6), 1458–1487 (1983).

19. V. I. Knauf, A. V. Mikolaichuk, and E. V. Khristov, "Structural Position of Mesozoic–Cenozoic Volcanism in the Central Tien Shan," in *Seismotectonics and Seismicity of the Tien Shan*, Ed. by K. E. Kalmurzaev (Ilim, Frunze, 1980) [in Russian].

20. D. L. Kohlstedt, B. Evans, and S. J. Mackwell, "Strength of the Lithosphere: Constraints Imposed by Laboratory Experiments," J. Geophys. Res. **100** (B9), 17 587–17 602 (1995).

21. N. V. Kondorskaya and N. V. Shebalin, *New Catalogue of Strong Earthquakes in the USSR from Ancient Times through 1977* (World Data Center A, Solid Earth Geophys., Boulder, 1982).

22. G. L. Kosarev, N. V. Petersen, L. P. Vinnik, and S. W. Roecker, "Receiver Functions for the Tien Shan Analog Broadband Network: Contrasts in the Evolution of Structures across the Talass-Fergana Fault," J. Geophys. Res. **98** (B3), 4437–4448 (1993).

23. V. N. Krestnikov and I. L. Nersesov, "Tectonic Structure of the Pamirs and the Tien Shan in Relation to the Moho Topography," Sov. Geol., No. 11, 36–69 (1962).

24. C. A. Langston, "Structure under Mount Rainier, Washington, Inferred from Teleseismic Body Waves," J. Geophys. Res. **84**, 4749–4762 (1979).

25. D. Li., D. Liang, C. Jia C., et al., "Hydrocarbon Accumulation in the Tarim Basin, China," AAPG Bull. **80** (10), 1587–1603 (1996).

26. D. Li, R. Gao R., D. Lu, et al., "Tarim Underthrust beneath Western Kunlun: Evidence from Wide-Angle Seismic Sounding," J. Asian Earth Sci. **20**, 247–253 (2002).

27. V. I. Makarov, *Neotectonic Structure of the Central Tien Shan* (GIN AN SSSR Proc. Issue 307) (Nauka, Moscow, 1977) [in Russian].

28. L. I. Makeyeva, L. P. Vinnik, and S. W. Roecker, "Shear-Wave Splitting and Small-Scale Convection in the Continental Upper Mantle," Nature **358**, 144–147 (1992).

29. N. Metropolis, M. N. Rosenbluth, A. W. Rosenbluth, et al., "Equation of State Calculations by Fast Computing Machines," J. Chem. Phys. **21**, 1087–1092 (1953).

30. P. Molnar and P. Tapponnier, "Cenozoic Tectonics of Asia: Effects of a Continental Collision," Science **189**, 419–426 (1975).

31. K. Mosegaard and M. Sambridge, "Monte Carlo Analysis of Inverse Problems," Inverse Problems **18**, 29–54 (2002).

32. E. A. Neil and G. A. Houseman, "Geodynamics of the Tarim Basin and the Tien Shan in Central Asia," Tectonics **16** (4), 571–584 (1997).

33. S. Oreshin, L. Vinnik, D. Peregoudov, and S. Roecker, "Lithosphere and Asthenosphere of the Tien Shan Imaged by *S* Receiver Functions," Geophys. Res. Lett. **29** (8) (2002) (doi:1029/2001GL014441).

34. Ch. Reigber, G. W. Michel, R. Galas, et al., "New Space Geodetic Constraints on the Distribution of Deformations in Central Asia," Earth Planet. Sci. Lett. **191**, 157–165 (2001).

35. S. Roecker, "Crust and Upper Mantle of the Kyrghyz Tien Shan: Constraints from Preliminary Analysis of GHENGIS Broadband Seismic Data," Geol. Geofiz. **42** (10), 1554–1565 (2001).

36. S. W. Roecker, T. M. Sabitova, L. P. Vinnik et al., "Three-Dimensional Elastic Wave Velocity Structure of the Western and Central Tien Shan," J. Geophys. Res. **98**, 15 779–15 795 (1993).

37. K. M. Scharer, D. W. Burbank, J. Chen, et al., "Detachment Folding in the Southwestern Tien Shan–Tarim Foreland, China: Shortening Estimates and Rates," J. Struct. Geol. **26**, 2119–2137 (2004).

38. A. M. C. Sengor, K. Burke, and J. F. Dewey, "Rifts at High Angles to Orogenic Belts: Tests for Their Origin and the Upper Rhine Graben as an Example," Am. J. Sci. **278**, 24–40 (1978).

39. E. Sobel and T. A. Dumitru, "Thrusting and Exhumation around the Margins of the Western Tarim Basin during the India–Asia Collision," J. Geophys. Res. **102** (B3), 5043–5063 (1997).

40. E. R. Sobel and N. Arnaud, "Cretaceous–Paleogene Basaltic Rocks of the Tuyon Basin, NW China and the Kyrgyz Tian Shan: The Trace of a Small Plume," Lithos. **50**, 191–215 (2000).

41. S. C. Thompson, R. J. Weldon, Ch. M. Rubin, et al., "Late Quarternary Slip Rates across the Central Tien Shan, Kyrgyzstan, Central Asia," J. Geophys. Res. **107** (B9) (2203) doi: 10.1029/2001JB000596 (2002).

42. G. Touissaint, E. Burov, and J.-P. Avuac, "Tectonic Evolution of Continental Collision Zone: A Thermomechanical Numerical Model," Tectonics **23** TC6003 (2004) doi:10.1029/2003TC001604.

43. Yu. A. Trapeznikov, E. B. Andreeva, B. Yu. Butalev, et al., "Magnetotelluric Soundings in the Kyrgyz Tien Shan," Fiz. Zemli, No. 1, 3–20 (1997) [Izvestiya, Phys. Solid Earth **33**, 1–17 (1997)].

44. L. P. Vinnik, A. M. Saiipbekova, and F. N. Yudakhin, "Deep Structure and Dynamics of the Tien Shan Lithosphere," Dokl. Akad. Nauk SSSR **268** (1), 143–146 (1983).

45. L. Vinnik, "Detection of Waves Converted from *P* to *SV* in the Mantle," Phys. Earth Planet. Inter. **15**, 39–45 (1977).

46. L. P. Vinnik, S. Chevrot, J.-P. Montagner, and F. Guyot, "Teleseismic Travel Time Residuals in North America and Anelasticity of the Asthenosphere," Phys. Earth Planet. Inter. **116**, 93–103 (1999).

47. L. Vinnik, H. Chenet, J. Gagnepain-Beyneix, and P. Lognonne, "First Seismic Receiver Functions on the Moon," Geophys. Res. Lett. **28** (15), 3031–3034 (2001).

48. L. Vinnik and V. Farra, "Subcratonic Low-Velocity Layer and Flood Basalts," Geophys. Res. Lett. **29** (4) (2002) (doi:10.1029/2001GL0144064).

49. L. Vinnik, D. Peregoudov, L. Makeyeva, et al., "Towards 3-D Fabric in the Continental Lithosphere and Asthenosphere: the Tien Shan," Geophys. Res. Lett. **29** (16) (2002a) (doi:10.1029/2001GF014588).

50. L. P. Vinnik, S. Roecker, G. L. Kosarev, et al., "Crustal Structure and Dynamics of the Tien Shan," Geophys. Res. Lett. **29** (22) (2002b) (doi:10.1029/2002GL015531).

51. L. P. Vinnik, Ch. Reigber, I. M. Aleshin, et al., Receiver Function Tomography of the Central Tien Shan," Earth Planet. Sci. Lett. **225**, 131–146 (2004).

52. C. J. Wolfe and F. L. Vernon, "Shear-Wave Splitting at Central Tien Shan: Evidence for Rapid Variation of Anisotropic Patterns," Geophys. Res. Lett. **25**, 1217–1220 (1998).